Ultrafast ionization and fragmentation of molecular silane

Scott G. Sayres,[1] Matt W. Ross,[1] and A. W. Castleman, Jr.[1,2,*]

[1]*Department of Chemistry, 104 Chemistry Research Building, Pennsylvania State University, University Park, Pennsylvania 16802, USA*

[2]*Department of Physics, 104 Chemistry Research Building, Pennsylvania State University, University Park, Pennsylvania 16802, USA*

(Received 6 January 2010; published 23 September 2010)

The ionization and fragmentation of molecular silane is examined here with laser intensities ranging between 7×10^{12} and 1×10^{15} W/cm^2 at 624 nm. The ionization potential of silane determined using both multiphoton ionization (MPI) and tunneling ionization (TI) models agrees with the vertical ionization potential of the molecule. In addition, the application of the tunneling ionization model is extended here to the fragments of silane to determine their appearance potentials. MPI values for SiH_3^+, SiH_2^+, SiH^+, Si^+, as well as H_2^+ and H^+ are consistent with vertical potentials, whereas the TI measurements are found to be in accord with adiabatic potentials. The tunneling appearance potentials observed for the fragments H_2^+ and H^+ are lower than reported for other techniques. In fact, the appearance potential measurements for these species resulting from silane are lower than their ionization potentials. The fragmentation rate of silane is determined to be nearly 20 times larger than the ionization rate. The main precursor for producing amorphous silicon (*a*-Si:H) thin films, SiH_3^+ is the dominant fragmentation product making up roughly a third of the total ion yield, a substantial increase from other techniques.

DOI: 10.1103/PhysRevA.82.033424 PACS number(s): 33.80.Rv, 33.15.Ry, 82.50.Hp, 42.50.Hz

I. INTRODUCTION

Elucidating the dynamics of ionization and concomitant fragmentation of molecules subjected to intense radiation is a topic of long-standing interest. Femtosecond laser pulses are known to remove electrons from molecules in a molecular beam on an ultrafast time scale, thus rapidly generating a plasma free of secondary collision reactions. This allows for observations of ionization potentials [1], ionization rates, branching ratios [2], as well as mechanistic pathways [3]. Femtosecond lasers can also be utilized to cause extreme ionization in molecules and clusters, producing multiply charged species much faster than the time required for significant nuclear rearrangement. The cations, created close together, repel one another resulting in a kinetic-energy release that propels the ions apart. This process is known as Coulomb explosion due to the forces between the cations driving them apart, and has been a main focus of some of our previous research [4–10]. For the experiment reported herein, specifically the strong-field excitation of silane, we are interested in examining the initial ionization processes over a range corresponding to both multiphoton ionization (MPI) and tunneling ionization (TI) mechanisms.

Plasma-enhanced chemical vapor deposition using silane gas has dominated the preparation of hydrogenated amorphous silicon (*a*-Si:H) thin films, which are used to create solar cells and thin film transistors [11,12]. Excitation of the weakly bound silane molecule results in the production of radicals, which are the film precursors. The properties of the resultant films have been found to strongly depend on the plasma conditions, leading to extensive information on of the plasma composition and reaction processes [12–19]. The reaction pathways of silane leading to these precursors have been studied in gas phase reactions [13–15] and also through electron-impact ionization [16–20]. The main objective of most research in this area has been in reducing the cost of thin film solar cells by raising the conversion efficiency of light to electric energy, and suppressing the degradation of the photoelectric properties of *a*-Si:H under long-time illumination [21].

The concentration of SiH_3^+ is directly responsible for the annihilation of defect sites on the *a*-Si:H film, which thereby increases conversion efficiency. However, SiH_3^+ is thought to be produced mainly through secondary collision reactions within the plasma [12]. To better understand the deposition process, it is critical to know the energy requirements, as well as the concentration, of the various ions in the plasma, especially the dominant film precursor, SiH_3^+. One way to improve the quality of the *a*-Si:H films is to enhance the concentration of SiH_3^+ in the plasma. Ionization induced by femtosecond lasers is examined as a way to increase the concentration of SiH_3^+.

Intense femtosecond lasers offer a unique way to examine the fundamental properties of a molecule where the laser field is comparable to the strength of the electron Coulomb binding potential. As laser intensity increases, the ionization mechanism changes from MPI to tunneling ionization according to the Keldysh parameter [22], $\gamma = \sqrt{(I_p/2U_p)}$, where I_p is the ionization potential and U_p is the ponderomotive potential of the laser. When $\gamma \ll 1$, the ionization process is dominated by field ionization, while $\gamma \gg 1$, ionization is dominated by MPI. The wide range in which γ is close to 1 is expected to have contributions from both processes. For a wavelength of 624 nm and an ionization potential of 12 eV, the Keldysh parameter is equal to 1 at a laser intensity of 1.65×10^{14} W/cm^2, which is centered within the range of intensities covered in this experiment.

TI has long been thought to be an attosecond ionization process, an assumption that has recently been verified [23]. Ionization occurs at the peaks of the electric field as it oscillates in the laser pulse envelope, as long as the intensity is sufficient. Although the ionization is an attosecond process, considered to be instantaneous with respect to nuclear motion, many cycle

*Author to whom correspondence should be addressed.

laser pulses allow for sequential ionization and some nuclear motion. Therefore, ion yields are typically determined using the adiabatic ionization potential for tunneling calculations [24].

Strong-field TI in noble gas atoms is well understood, and theoretical models are even able to predict the resultant ion signal for sequential ionization to higher charge states. For this reason, the noble gases are often used to calibrate the intensity of a laser for measurement against other molecules. Ultrafast TI dynamics are more complicated in molecules. The well-known Ammosov-Delone-Krainov (ADK) [25] model has been applied to a variety of molecules with limited success, however, it is still the preferred tunneling model due to its simplicity and relative accuracy. Fragmentation and Coulomb explosion can occur in molecules leading to deviations from the expected ion signal [24,26]. The ADK model overestimates ionization rates, thereby predicting saturation intensities lower than the measured values for many organic molecules [24] as well as some transition metal species [27]. ADK theory employs the single active-electron theory (SAE), and so multiple active electrons have been examined as a way to explain some of the deviations [28]. The orientation of the molecule with respect to the laser polarization also affects the observed tunneling rate [29]. Finally, molecular orbitals have been included as a way to account for the ionization suppression [30,31].

There have been very few studies focused on the treatment of fragments in the strong field to determine the energy requirements for their production [2]. In the present experiment, we determine the laser intensity required for silane to ionize and fragment using a femtosecond laser with intensities ranging from $\sim 10^{13}$ to $10^{15}\,\mathrm{W/cm^2}$. Models of both MPI and TI are applied to silane to determine the ionization potential, and to its fragments to determine appearance potentials. The appearance potential is defined as the minimum amount of energy required for the production of a certain fragment. Finally, we compare these observed values to those reported from other experimental techniques including electron-impact ionization (EI) as well as photon ionization (PI). Mass spectrometry is utilized to determine the ion concentrations of the fragments.

II. EXPERIMENTAL TECHNIQUE

This experiment was performed with a z-scan technique known as intensity selective scanning (ISS) in which changes in ion yield are examined as a function of laser intensity [32–36]. Attenuation of the laser intensity was performed through translation of a 60 cm focusing lens in the direction of the laser beam, so that the beam waist changes as it intersects the molecular beam. The ion signal was then collected using a home built, single stage Wiley-McLaren [37] time-of-flight mass spectrometer where the electrostatic grids were replaced with metal plates having a 2.00 mm slit perpendicular to the laser direction. Careful attention was paid to ensure that the slit was smaller than the Rayleigh range of the laser, limiting the ion collection from the interaction of the laser and sample to a finite slice of nearly constant laser intensity. Translation of the lens was controlled with a step size of 100 μm and a resolution of ± 1 μm. This technique offers the advantage of collecting a large volume of ion signal at low laser intensities, where the ionization probability is small and dominated by MPI [33]. This is especially beneficial in studying the transition between MPI and TI, where we are interested in low-intensity interactions leading to fragmentation, as opposed to multiply charged species.

A gas mixture of 1% silane seeded in helium was introduced into a vacuum chamber through a needle valve, placed 1 cm directly above the extraction region of the mass spectrometer equipped with plates held at static voltages. The vacuum chamber pressure was maintained at 1×10^{-6} Torr. Cations, created during the interaction of the ionizing laser with the effusive gas jet are accelerated toward a meter-long field-free region. After being steered by an Einzel lens, they are detected with a chevron stack of MCPs coupled to an oscilloscope and computer for analysis.

Laser beam parameters were well characterized before entering the vacuum chamber and interacting with the molecular beam. A previously described colliding-pulse ring cavity mode-locked dye laser [3], centered at 624 nm, with average energy of 0.75 mJ per pulse and a pulse having a full width at half maximum (FWHM) of 100 femtoseconds (fs) was used to interrogate the silane molecule perpendicular to the ion flight path. The pulse width was measured both with single-shot autocorrelation as well as interferometric autocorrelation. The beam energy was measured using a Molectron pyrometric energy meter. The focused beam waist was determined by knife-edge profiling [38] to be 2.38×10^{-5} m, delivering a peak intensity of $\sim 1 \times 10^{15}\,\mathrm{W/cm^2}$.

III. THEORETICAL MODELS

A. *Ab initio*–DFT calculations

Ab initio calculations were performed within the Gaussian 03 program package [39]. The geometry optimizations and energies were carried out using an unrestricted hybrid method that includes a mixture of Hartree-Fock (HF) exchange with density functional exchange correlation using 6–311++G(3*df*, 3*pd*) basis sets. The exchange and correlation integrals were treated with the generalized gradient approximation of Becke's three parameters [40] and the dynamic Perdew and Wang's 1991 [41] gradient-corrected correlation functional (B3PW91). The final energies were determined using the *ab initio* singles and doubles coupled-cluster method (CCSD) [42–45]. The ground-state structure was found to be a perfect tetrahedral with Si-H bond length of 1.48 Å and H-Si-H bond angle of 109.471°. Contour plots of the molecular orbitals at an isosurface value = 0.02 were drawn using the MOLEKEL program [46] and are displayed in Fig. 1.

To better understand the mechanisms leading to products, the fragmentation energies were calculated via

$$E_{\mathrm{reaction}} = \sum E_{\mathrm{products}} - \sum E_{\mathrm{reactants}}. \qquad (1)$$

These calculations are performed to obtain vertical energies for which experimental and theoretical data in the literature are lacking. The vertical energies were calculated with structures having no nuclear rearrangement, hence for a frozen geometry. Adiabatic energies were calculated with species fully relaxed to their ground-state geometries. Relevant mechanisms and

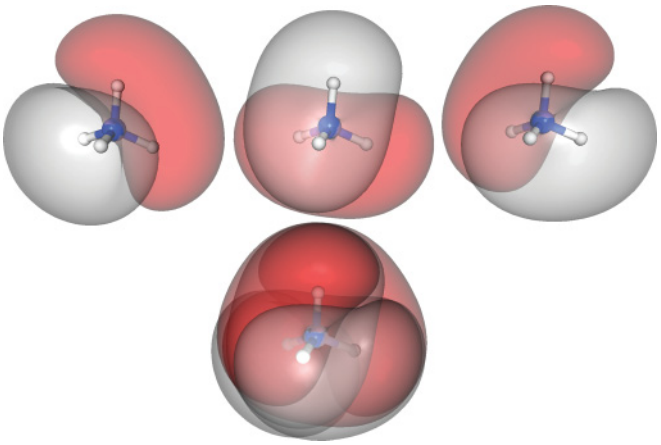

FIG. 1. (Color online) Contour plots of the HOMO of silane at an isosurface value = 0.02. The HOMO is made up of three degenerate $2t_2$ orbitals (top) which are overlapped (bottom) to demonstrate the spherical geometry of the orbital.

their energies are displayed in Table I. The lowest spin state was found to be the lower energy state for all structures and so are the only ones reported. Experimentally determined appearance potentials using both MPI and TI models are compared to these energies to gain insight into the mechanism.

B. ADK model

The well-known ADK tunneling model [25] was used to calculate the static ionization rate as

$$W_{\text{stat}} = \frac{\kappa^2 [C_{n^*\ell} Q(\ell,m)]^2}{2^{|m|}(|m|)!} \left(\frac{2\kappa^3}{F}\right)^{2n^*-|m|-1} e^{-2\kappa^3/3F}, \qquad (2)$$

where

$$C_{n^*\ell} = \left(\frac{2e}{n^*}\right)^{n^*} \frac{1}{\sqrt{2\pi n^*}},$$

and

$$Q(\ell,m) = (-1)^{(m+|m|)/2} \sqrt{\frac{(2\ell+1)(\ell+|m|)!}{2(\ell-|m|)!}}.$$

The rate is dependent on the ionization potential I_p, the laser's electric field amplitude F, the effective angular ℓ, magnetic m, and effective principal $n^* = Z_c/\kappa$ quantum numbers. Z_c represents the charge state after the electron departs $\kappa = \sqrt{2I_p}$ and e represents Euler's number. Atomic units ($m = \hbar = e = 1$) are used throughout this paper unless otherwise noted.

To apply the ADK model to molecules, knowledge of the angular and magnetic quantum number of the active electron must be obtained. These values can have a dramatic effect on the ionization rate, but have been largely ignored for simplicity. With the assumption that the relaxation rate of higher-order magnetic numbers is much faster than the ionization rate, m is commonly set to 0 because the ionization rate of $m = 0$ is much greater than of $|m| > 0$. The top of Fig. 1 shows three degenerate $2t_2$ filled orbitals combined to form a nearly spherical orbital (bottom of the figure) having 60% s-wave and 40% p-wave contributions. An angular momentum quantum number of 0 is used in our ADK calculations due to the dominant s-wave contribution to the highest-occupied molecular orbital (HOMO).

TABLE I. Relevant reaction pathways as calculated for a frozen geometry as well as an adiabatically relaxed geometry. Also shown are threshold energy (E_{th}) values collected in the literature for comparison to the calculations performed in this work for adiabatic pathways. The table is broken into three parts: fragmentation channels of silane leading to ionized products, fragmentation channels of neutral silane fragments that result in cation products, and silane fragmenting to neutral products. All energy values are given in eV.

Reaction Pathway	Frozen E	Relaxed E	E_{th}^{a}
$SiH_4 \rightarrow SiH_4^+$	12.84	11.37	11
$SiH_4 \rightarrow SiH_3^+ + H$	13.04	12.12	12.03
$SiH_4 \rightarrow SiH_2^+ + H_2$	16.17	11.60	11.57
$SiH_4 \rightarrow SiH_2^+ + 2\,H$	16.36	16.30	
$SiH_4 \rightarrow SiH^+ + H + H_2$	18.35	13.82	13.73
$SiH_4 \rightarrow SiH^+ + 3\,H$	18.53	18.53	
$SiH_4 \rightarrow Si^+ + 2\,H_2$	21.50	12.47	12.47
$SiH_4 \rightarrow Si^+ + H_2 + 2\,H$	21.69	17.18	
$SiH_4 \rightarrow Si^+ + 4\,H$	21.88	21.88	
$SiH_4 \rightarrow H^+ + SiH_3$	17.74	17.73	17.61
$SiH_4 \rightarrow H_2^+ + SiH_2$	20.24	18.14	18.07
$SiH_3 \rightarrow SiH_2^+ + H$	12.21	12.17	12.09
$SiH_3 \rightarrow SiH^+ + H_2$	14.23	9.69	9.72
$SiH_3 \rightarrow Si^+ + H_2 + H$	17.58	13.05	12.99
$SiH_3 \rightarrow H^+ + SiH_2$	17.04	16.79	16.76
$SiH_2 \rightarrow SiH^+ + H$	11.21	11.21	11.19
$SiH_2 \rightarrow Si^+ + H_2$	14.21	9.85	9.83
$SiH_3 \rightarrow SiH_3^+$	8.74	8.98	8.01
$SiH_2 \rightarrow SiH_2^+$	9.40	8.98	8.92
$SiH \rightarrow SiH^+$	7.82	7.81	7.91
$H_2^* \rightarrow H_2^+$ (2.41 Å)	12.91	11.00	15.43
$H_2 \rightarrow H_2^+$ (0.74 Å)	16.40	15.52	15.43
$SiH_4 \rightarrow SiH_2 + H_2$	7.34	2.62	
$SiH_4 \rightarrow SiH_3 + H$	4.14	4.13	

[a]Reference [20].

C. MO-ADK model

Several years ago, the ADK model was further developed for application to multiatom species [31]. The introduction of MO-ADK theory allowed the TI rate to be calculated at any alignment for a molecule with respect to the laser field. Electrons are assumed to tunnel through only a small cone of angles aligned with the laser polarization. The ionization rate can now be expressed as a summation of partial wave contributions as follows:

$$W_{\text{stat}}(F,R) = \sum_{m'} \frac{|B(m')|^2}{2^{|m'|}|m'|!} \frac{1}{\kappa^{2n*-1}} \left(\frac{2\kappa^3}{F}\right)^{2n*-|m'|-1} e^{-2\kappa^3/3F}, \qquad (3)$$

where $B(m') = \sum_{\ell,m} C_{\ell m} D^{\ell}_{m',m}(R) Q(\ell,m')$.

In Eq. (3), $D^{\ell}_{m',m}(R)$ is Wigner's rotation matrix [47,48], m' is used to designate the laboratory frame orientation, and R denotes Euler angles (ϕ,θ,χ) between the molecular axis and the field direction, where ϕ and χ correspond to rotations about the space-fixed Z axis and the body fixed z axis, respectively, while θ represents the angle between the Z and z axis. We only

consider a linearly polarized laser pulse, which is independent of ϕ, the angle of rotation around the polarization vector.

The rate is strongly dependent upon the molecular orbital fitting coefficients, $C_{\ell m}$. In our determination of these coefficients, we have adopted a procedure [49,50] in which the HF molecular wave function, containing diffuse orbitals, is compared to asymptotic Coulomb waves. The HOMO, obtained from the Gaussian software package, is separated into angular and radial components, expressed as

$$\Phi_0(r) = \sum_{\ell} \sum_{|m| \leqslant \ell} F_{\ell m}(r) Y_{\ell m}(\hat{r}), \tag{4}$$

where $Y_{\ell m}(\hat{r})$ are the usual spherical harmonics describing the angular part and $F_{\ell m}(r)$ are radial functions. The radial functions can be determined using the orthogonality of spherical harmonics. Knowledge of the radial and angular functions allows for an exact reproduction of the original wave function. A one-center expansion is performed to determine the radial functions, and the complex coefficients $C_{\ell m}$ are determined as scalars matching the radial functions to asymptotic Coulomb waves of the form

$$F_{\ell m}(r \to \infty) \to C_{\ell m} r^{Z/\kappa - 1} e^{-\kappa r}, \tag{5}$$

in the radial range of 6 to 10 a.u. The decay of the Gaussian-type orbitals used in our HF wave function are not accurate at distances much larger than this. It is sufficient to determine $C_{\ell m}$ at only one orientation, as they too can be rotated by the Wigner rotation function [51]. We have determined the complex fitting coefficients for the three degenerate molecular orbitals of silane, which are negligible above $\ell = 6$ [52].

D. Cycle-averaged rate

In either formulation [Eqs. (2) or (3)], the cycle-averaged ionization rate must be determined to account for the oscillatory laser field. Additionally for molecules, the ionization rate may be different with respect to the polarity of the laser field. The ionization rate in the negative direction W^-, can be determined with the use of the parity operator, which transforms the coefficients by substituting $C_{\ell m}$ with $(-1)^l C_{\ell m}$ in Eq. (3). In the original ADK model, W^+ is equal to W^-. Therefore, the cycle-averaged ionization rate W is computed from the ionization rate as follows:

$$W = \left(\frac{3F}{\pi \kappa^3}\right)^{1/2} \frac{W^+ + W^-}{2}. \tag{6}$$

In our experiment, the molecule can be oriented in any random direction with respect to the laser. Therefore an average over a distribution corresponding to all alignments is needed. The ionization rate is then scaled by the number of electrons occupying the molecular orbital, or in this case, each orbital is multiplied by 2. Finally, the degeneracy of the HOMO allows three molecular orbitals to contribute equally to the ionization and therefore the rate from each orbital must be accounted for. At every orientation, the maximum value from the three orbitals is used as the molecule's ionization rate. Figure 2 shows the ionization rate at every orientation for each of the degenerate HOMO's individually, as well as their combination.

We have calculated the MO-ADK ionization rate for silane using Eqs. (3) and (6), and compared it to the atomic theory

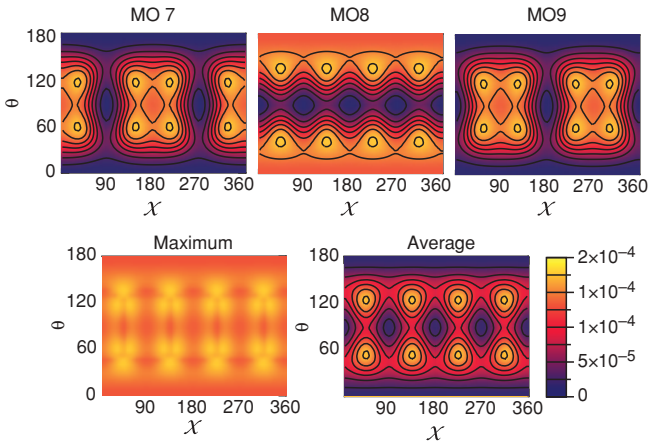

FIG. 2. (Color online) Mercator projection plots showing the alignment-dependent ionization rate for the three degenerate $2t_2$ orbitals of silane as calculated through MO-ADK theory at a laser intensity of 1×10^{14} W/cm^2. The degeneracy of the orbitals allows them all to contribute equally to the ionization rate. The maximum value from the three orbitals at every angle is used as the molecule's ionization rate, leading to a nearly constant rate at all angles. The three orbitals are also averaged to demonstrate the symmetry.

using Eqs. (2) and (6). The MO-ADK model yields a rate that is approximately equal to the ADK model, and therefore the agreement is excellent at intensities below 1×10^{15} W/cm^2 as shown in Fig. 3. Above this intensity, the MO-ADK ionization rate grows exponentially with respect to the atomic model. However, this is inconsequential because this not only corresponds to intensities above the upper limit from the laser, but also enters the regime in which over the barrier suppression ionization is the dominant mechanism meaning that tunneling equations are not appropriate. Thus, the use of the atomic ADK rate for an s orbital is accurate for this tetrahedral molecule,

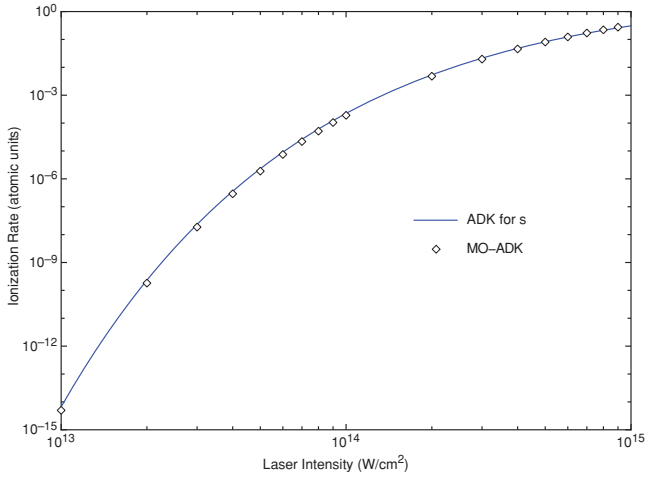

FIG. 3. (Color online) Ionization rate (in atomic units) as a function of laser intensity over the range explored in this experiment. The solid (blue) line is calculated using atomic ADK theory [Eqs. (1) and (4)] for an $\ell = 0$ orbital. The diamond data points indicate the ionization rate calculated through MO-ADK theory for silane averaged over all orientations and multiplied by two to account for electron occupancy.

allowing the HOMO to be approximated as if it where perfectly spherical.

Our calculations show that for the laser intensities used here, the largest ionization rate comes from a molecule whose orbital is aligned with the laser. Similar to N_2, there is a decrease in ionization rate as the molecular alignment is varied so that the bonds are not aligned with the laser [30,31]. Therefore because the strongest ionization occurs with alignment, no ionization suppression is expected.

The probability P of ionizing an electron is related to the ionization rate and is dependent upon the pulse width of the laser, represented by

$$P = 1 - e^{-\int_{-\infty}^{\infty} W dt}. \tag{7}$$

Using a square-wave laser pulse for simplicity reduces the integral to $W\tau$, where τ is the pulse width of the laser [24].

E. Ion signal from Gaussian laser pulse

By varying the laser intensity, measurements can be made of the ionization mechanism of a species by measuring the ion signal that is produced. The measured ion signal is a function of the ionization rate, interaction volume, instrument sensitivity, and concentration [24]. Therefore the ionized signal must be integrated with respect to laser intensity and volume.

The focal volume of the laser beam is calculated assuming a Gaussian beam profile. The beam waist $w(z)$ at any distance from the focus z can be calculated using

$$w(z) = w_0\sqrt{1 + \left(\frac{z}{z_r}\right)^2}. \tag{8}$$

In Eq. (8), the Raleigh length $z_r = \pi w_0^2/\lambda$, is used to approximate the distance for which the energy of the beam remains roughly the same and w_0 is the minimum beam waist. The peak intensity I_{peak}, at any distance can be calculated as

$$I_{\text{peak}}(z) = \frac{2L_P}{\pi w(z)^2}, \tag{9}$$

where L_P is the laser power in watts.

The volume V of the Gaussian laser pulse selected by the slit with intensity I greater than an isointensity curve I_0 must be calculated accurately using

$$V = \frac{\pi}{2} w_0^2 \Delta z \left[1 + \left(\frac{z}{z_r}\right)^2\right] \ln\left(\frac{I_{\text{peak}}}{I_0\left[1 + \left(\frac{z}{z_r}\right)^2\right]}\right), \tag{10}$$

where the slit width is represented by Δz [32,35,36].

Both volume and probability are dependent on the intensity of the laser. Assuming a uniform distribution of molecules across the laser's volume, the ion signal S for a given slice is calculated [36] by integrating the laser parameters with respect to intensity

$$S = \alpha c \int_0^{I\text{peak}} \frac{\partial V}{\partial I} P dI, \tag{11}$$

where scaling factors are ion concentration c and instrumental sensitivity α [24].

F. Multiphoton ionization

Atomic species undergoing MPI through nonresonant photon absorption can be explained using lowest-order perturbation theory [53]. Using low laser intensities, the number of photons absorbed for an electronic transition can be determined from a plot of an ion signal as a function of laser intensity. The rate of ionization for a nonresonant MPI with a coherent laser pulse is given by

$$W = \sigma_N I^N, \tag{12}$$

where σ_N is the ionization cross section and N is the number of photons necessary for ionization to take place. Taking the logarithm of both sides of Eq. (12) leads to the following equation, where the slope of the straight line is equal to N:

$$\log_{10}(W) = N \log_{10}(I) + \log_{10}(\sigma_N). \tag{13}$$

This oversimplified equation is only valid when the ionization probability is much less than unity as saturation effects decrease the measurement of the slope. Resonance effects also lowers the slope measurement from the expected value. In practice, it is often difficult to obtain accurate measurements as the ion signal at low laser intensities can be lost in the background noise. The effects of TI may already be present when the ionization signal is large enough for detection. Therefore, the measurements often present a lower bound limit for the photon requirement [53]. Noninteger values for the photon order are indicative of a more complex mechanism occurring, including the effects of resonance with intermediate states and fragmentation [54]. Although this model is designed to determine the number of photons absorbed, the slope is used here to approximate the appearance potential.

As mentioned previously, this model is only accurate when the Keldysh parameter is much greater than 1. The transition of where MPI, and thus perturbation theory, fails to describe the ionization dynamics is still not well understood, but shows dependence upon both pulse width and wavelength. The accurate measurement of the photon order for even a noble atom can be difficult. Using a 100 fs laser at 780 nm, the ion yield of He was measured over 11 orders of magnitude in an ion signal [55]. The lowest laser intensity in which an ion signal was observed, 8×10^{13} W/cm^2, corresponds to a Keldysh parameter of 1.65, suggesting MPI was the dominant mechanism. However, the measured maximum slope yields a value of ~15.5 eV, demonstrating that a larger Keldysh parameter is necessary to obtain accurate photon orders under these conditions. A separate experiment using 40 ps pulses at 532 nm enabled measurement of the correct slope (11 photons) over a Keldysh parameter between ~6.83 and 4.83 (1×10^{13} and 2×10^{13} W/cm^2) [56].

IV. RESULTS AND DISCUSSION

The saturation intensity, I_{sat}, of an ion has been shown to be a consistent measure of the ionization potential when related to TI, and is defined as the intersection of the laser intensity axis and the straight line of the ion yield extrapolated back from the high intensity on a semilog plot [24]. I_{sat} is a function of the pulse width of the laser and also the slit diameter, so similar

conditions must be employed to compare molecules. The laser intensity was first calibrated by matching the saturation intensity of atomic xenon to the ADK determined value, which is known to be in agreement. For the laser conditions employed in this experiment, the ion signal calculated through the ADK model for Xe match an effective square wave pulse width of 100 fs and a linear extraction value I_{sat} of 5.81×10^{13} W/cm^2.

A. Ionization of silane

To determine the ionization potential for other molecules, the experimentally measured I_{sat} is compared to the theoretically determined I_{sat} of a virtual atom with various ionization potentials using ADK equations until agreement is reached. The determination of the I_{sat} for molecular silane is shown in Fig. 4(a) as an example. The I_{sat} for silane is determined to be 6.92×10^{13} W/cm^2, which corresponds to a virtual atom with an ionization potential of 12.88 eV according to ADK simulations. Thus, the ionization potential of silane is

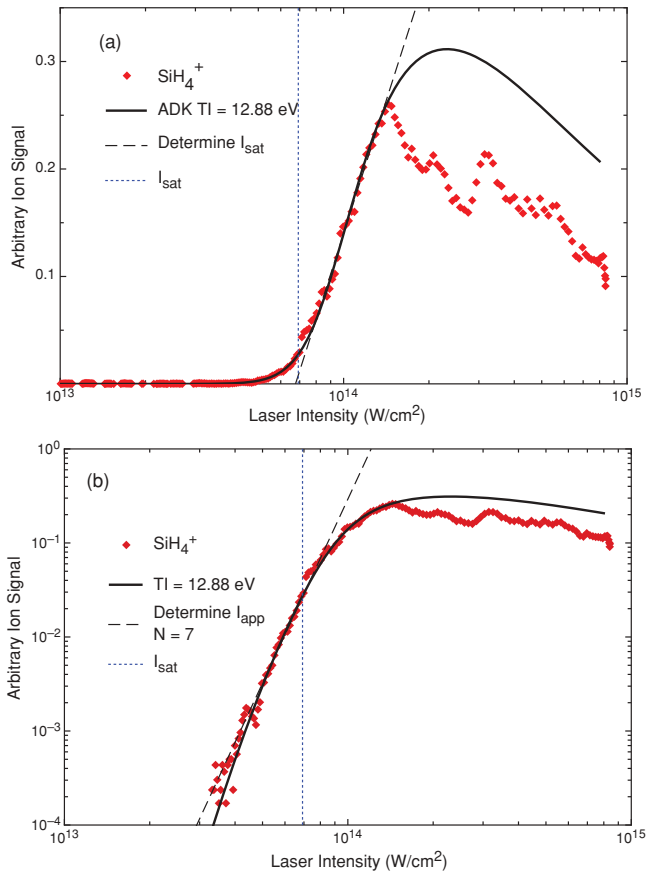

FIG. 4. (Color online) (a) Ion yield as a function of laser intensity on a semilog plot to determine the saturation intensity of SiH_4^+. See text for details. (b) Logarithmic plot to find the appearance intensity of SiH_4^+. The (red) diamonds indicate experimental data points. The dashed line (black) is used to determine I_{app}, and has a slope listed N. The dotted (blue) vertical line indicates I_{sat}. The solid (black) line shown in both graphs is the calculated ion signal corresponding to the matching saturation intensity using the ADK model.

12.88 eV as determined through TI. Deviation of the SiH_4^+ signal from the calculated ADK curve above 1×10^{14} W/cm^2 is attributed to how unstable the molecule is. The molecule undergoes fragmentation depleting the ion signal from the calculated curve.

The appearance intensity I_{app} demonstrates the minimum laser intensity required for a given ion to be detected by the instrument. It is determined by fitting a line to the low-intensity signal in a log-log plot of the ion signal versus laser intensity and then extrapolating the line to the minimum signal discernible from the baseline noise, which in this case is 1×10^{-4} volts on the oscilloscope. I_{app} can be thought of as an upper limit to the energy requirements for the creation of an ion because it is affected by ion concentration and detection efficiency. Thus the actual energy requirements for producing a given ion could be lower, but the ion signal is too low to be detected above the background noise. More important is the slope measured for the log-log plot at very low intensities, where MPI dominates ionization according to the Keldysh parameter. The slope indicates the number of photons involved in the generation of ion signal. In Fig. 4(b), the initial ion signal, measured at Keldysh parameters between 2.43 and 1.60, has a slope of 7. This suggests that the ionization potential for silane, according to MPI, is 13.93 eV (7×1.99 eV).

Due to the instability of the molecule, it is difficult to obtain a definitive measurement of the vertical ionization potential. Multiple EI studies have specifically stated the absence of SiH_4^+ [16,17,19,57]. One study from EI, measured a value of 12.4 eV [58]. The vertical ionization potential has been estimated at 12.4 eV [59] from dipole (e,e) spectroscopy; explained as arising from Jahn-Teller distortions splitting the valence electrons into three electronic orbitals with energies 12.4, 12.82, and 13.24 eV [60,61]. These splittings were then confirmed with photoelectron spectroscopy as 12.3, 12.8, and 13.1 eV [62]. Photoelectron spectroscopy determines the initial value to be 12.82 eV [63]. The calculated values lie mostly in the range between 12.3 and 12.88 [64] eV. In our TI measurements, the ion signal corresponds to an ionization potential of 12.88 eV according to ADK theory. The slope taken from MPI indicates a vertical potential between 11.94 and 13.93 eV. Both of the measurements are in agreement with previously measured values. The TI potential for molecular silane matches closely to the vertical value, suggesting that nuclear rearrangement leads to fragmentation and therefore does not contribute to this measurement. Our CCSD calculation of 12.84 eV shown in Table I is also in agreement with the range in values.

B. Fragmentation of silane

In many cycle laser pulses, the ionization mechanism can be complicated and difficult to determine. Differentiating between a mechanism involving first the direct ionization of the molecule leading to dissociation (vertical excitation) and another mechanism involving the rearrangement of the molecule followed by ionization (adiabatic excitation) requires knowledge of the energy states involved. In order for the laser to drive the process, all steps in the mechanism requiring excitation must occur faster than the laser's pulse width, while the electric field of the laser is still present to progress the

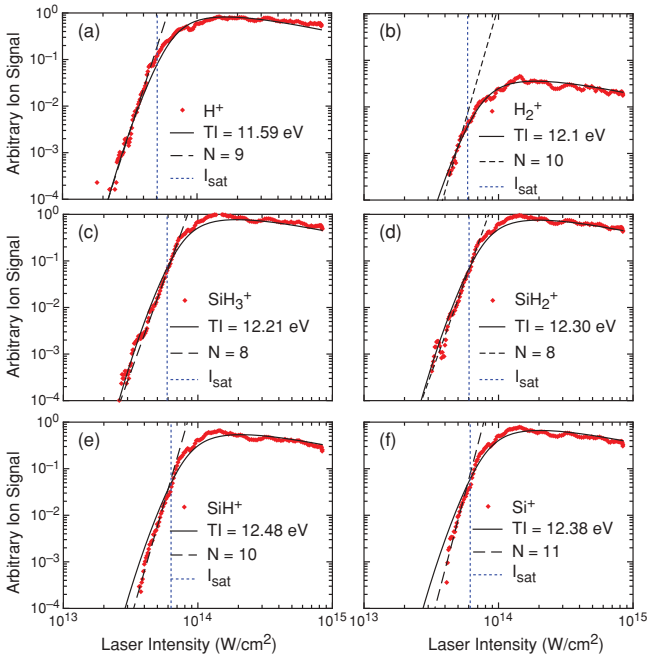

FIG. 5. (Color online) (a)–(f) Ion yields for the fragments of silane as a function of laser intensity on a log-log plot. The (red) diamonds indicate experimental data points and the vertical (blue) dotted lines indicate the saturation intensity for each species. The solid (black) line indicates the ion yield calculated through the ADK model according to the ion potentials measured at the I_{sat}. The dashed (black) line indicates the best fit line in which the slope N is used to determine the number of photons required.

reaction. Subsequent relaxation or dissociation may occur after the laser pulse has passed.

The half period, or time between peak amplitudes of the electric field of our laser pulse is 1.04 fs, allowing for very small nuclear rearrangements between peaks. As the geometry of the molecule evolves, it is subject to many peak amplitudes and excitation will occur if the energy gap between states is overcome through tunneling. If nuclear rearrangement occurs on the time scale of the laser pulse, the application of the TI model allows for the determination of the minimum energy requirement, or appearance potentials for the fragment ions. If rearrangement requires more time than is available, the state will not be observed until higher laser intensity is applied. Taking measurements for the fragments in the same manor as discussed previously for molecular silane provides insight into the energy requirements and time scales for the various fragmentation pathways.

In Figs. 5(a) through 5(f) the ion signal for all fragments of silane (specifically H^+, $H_2{}^+$, $SiH_3{}^+$, $SiH_2{}^+$, SiH^+, and Si^+, respectively) are shown on a log-log plot to demonstrate the measurements using both TI and MPI models. The initial slopes are taken as a determination of the photon order. The I_{sat} value, used in the TI model, is shown as a dotted vertical blue line. The corresponding appearance potential from TI is then plotted to show its agreement with the data. The application of these models to the fragments shall now be discussed individually.

1. Multiphoton model

The dissociation rate of silane is greater than the ionization rate, leading to extensive fragmentation at the intensities in this experiment. The onset ion signal is fit to integer slopes, giving insight into the amount of energy required for the appearance of a fragment or ion. The slopes determined from the plots in Figs. 4 and 5 as well as the corresponding appearance potentials for each of the fragments are summarized in Table II.

MPI performed with a femtosecond laser is expected to occur according to vertical transitions, as photon absorption is much quicker than nuclear rearrangement. Therefore the measured MPI values are compared only to vertical calculations through a frozen geometry. The slope for both $SiH_3{}^+$ and $SiH_2{}^+$ is measured at 8, demonstrating an apparent potential of 15.92 eV. For $SiH_3{}^+$, this is one photon higher than the CCSD calculation suggests at 13.04 eV. $SiH_2{}^+$ can be produced through vertical excitation following two pathways as shown in Table I. The first mechanism is the loss of an excited hydrogen molecule ($SiH_4 \rightarrow SiH_2{}^+ + H_2$) calculated at 16.17 eV, and the second is the loss of two hydrogen atoms simultaneously ($SiH_4 \rightarrow SiH_2{}^+ + 2\,H$) calculated at 16.36 eV. Our measurement cannot distinguish between the two mechanisms, as they both require 9 photons.

The production pathways of SiH^+ and Si^+ from silane are more complicated as they result in a minimum of three fragments from the mechanism, necessitating that more than one bond be broken. Therefore, it is not surprising for the measurements to deviate slightly from the theoretical values. A low laser intensity signal from SiH^+ is measured with a slope of 10, leading to an appearance potential of 19.9 eV according to MPI. This is the correct photon order according to the CCSD calculation for a mechanism resulting in the loss of H_2 and H (18.35). The measured slope of 11 for Si^+ indicates an appearance potential in the range of 21.89 eV, which is fairly close to the three fragmentation mechanisms listed in Table I. The removal of two H_2 requires 21.50 eV, the loss of H_2 and two H requires 21.69 eV, and the loss of four H requires 21.88 eV.

H^+ is calculated to appear as a product of silane at only 17.74 eV, in excellent agreement to the measured slope of 9 through MPI, or an appearance potential of 17.91 eV. The appearance potential for $H_2{}^+$ was calculated to be 20.24 and was measured at a slope of 10, which is in agreement. All of the measured values match closely to calculations of the frozen geometry excitation of neutral silane indicating that significant nuclear rearrangement does not occur during MPI with a femtosecond laser.

2. Tunneling model

As shown in Fig. 5, the calculated TI signal does not deviate from the experimental signal at high intensities for any of the fragments. This is in contrast with the molecular silane signal, and indicates that the ions do not undergo further fragmentation at these intensities. The ADK calculation also agrees well with ion signal at low intensities where MPI is expected to dominate according to the Keldysh parameter. The ADK calculation only slightly overestimates the ionization rates for SiH^+ and Si^+ below their respective saturation intensities.

TABLE II. Experimental measurements of I_{app}, I_{sat}, and the appearance potentials from ADK theory for TI. The photon order and potential for MPI are also listed. Appearance potentials measured from EI and PI are used for comparison. The normalized fragmentation branching ratios only include ions that contain a silicon atom.

	SiH_4^+	SiH_3^+	SiH_2^+	SiH^+	Si^+	H_2^+	H^+
I_{app} (10^{12} W cm^{-2})	30.8	26.6	27.0	33.3	33.3	38.3	21.7
I_{sat} (10^{12} W cm^{-2})	69.2	59.1	60.4	63.2	61.6	58.9	50.6
I_{sat}/I_{app}	2.25	2.22	2.24	1.90	1.85	1.54	2.33
AP from TI (eV)	12.88	12.21	12.30	12.48	12.38	12.19	11.59
AP EI[a] (eV)	N/A	12.2	11.6	15.01	13.56	24.3	24.5
AP PI (eV)	11[b](12.82)[c]	12.09[b]	11.52[b]	13.8[d]	N/A	N/A	N/A
EI/TI	1.00	1.00	0.94	1.20	1.10	1.99	2.11
Vertical IP	12.84	13.04	16.17	18.35	21.50	20.24	17.74
IP/hν	6.45	6.55	8.12	9.22	10.80	10.17	8.91
Measured N	7	8	8	10	11	10	9
Branching Ratio (%)	6	30	27	16	20	–	–

[a]Reference [17].
[b]Reference [61].
[c]Vertical IP obtained from Ref. [63].
[d]Reference [57].

The vertical energies determined through DFT calculations for the fragments are all much higher than measured through TI, indicating that nuclear motion plays a large role in the strong-field ionization of silane for many cycle light pulses. This is in agreement with previous experiments that use the adiabatic ionization potential for calculations of the tunneling rate. Experimental values obtained from EI and PI mechanisms are used for comparison with the measurements from the adiabatic TI model. The I_{app} and I_{sat} measured in Figs. 4 and 5, as well as the corresponding appearance potential from the TI model, are also shown in Table II. Literature values from other experiments are also given to determine the accuracy of the measurements. The ratio between I_{sat} and I_{app} is nearly 2:1 for all species.

The measured appearance potential for SiH_3^+, 12.21 eV, is only slightly higher than reported for either EI, 12.2 eV [17], or PI, 12.086 eV [61], experiments. The adiabatic calculation yields 12.12 eV, which is in excellent agreement. Therefore, we conclude that SiH_3^+ is produced adiabatically from neutral silane during tunnel ionization.

SiH_2^+ is the only fragment with a measured potential, 12.30 eV, that is higher in energy than the values reported for either EI, 11.6 eV [17], or PI, 11.52 eV [61]. The sequential loss of two hydrogen atoms is calculated to be 16.36 eV, but the rearrangement bringing the two H together to yield H_2 at 11.60 eV is in much better agreement with our measurement, making it the likely mechanism. We suggest two mechanisms to explain the deviation in the experiment and theory. First, the silane molecule requires more time than available during our pulse envelope to fully relax to the stretched geometry, and consequently fragmentation occurs at an energy requirement between the frozen and adiabatic values. An alternative explanation is that the hydrogen atom, whose bond is aligned with the electric field of the laser, is preferentially removed as its ionization rate will be higher than the other molecular orbitals. The fragmentation energy before any rearrangement has been calculated to be only 4.14 eV as seen in Table I. Neutral SiH_3 then undergoes an additional reaction with the laser pulse and fragments to form SiH_2^+ at only 12.17 eV. This two-step mechanism, involving the sequential loss of hydrogen atoms during ionization, matches our measurement. The term "fragmentation" must be used with caution, as separation of the two products is limited during the laser pulse. Therefore, the real mechanism is most likely a convolution of the mechanisms suggested, in which stretching of the aligned bond influences the fragmentation reaction.

The ion signals from SiH^+ and Si^+ match the appearance potentials of 12.48 and 12.38 eV, whereas the EI values measure 15.01 and 13.5 eV [17], respectively. PI sets these values slightly lower at 13.8 [57] and 12.65 eV [61], which is in much better agreement with the experimental measurements. Table I shows that only one pathway is close in energy to the measurement for each ion. Si^+ is produced when two H_2 molecules are removed from silane at an appearance potential of 12.47 eV, which is in agreement with our measurement. SiH^+ is produced as silane loses H_2 and H requiring 13.82 eV. To explain the deviation observed in SiH^+, we again explore a multistep pathway. silane is a very weakly bound molecule, requiring only ~4 eV to fragment as listed in Table I. The resultant SiH_3 or SiH_2 species can be excited to yield SiH^+ at 9.69 or 11.21 eV, respectively. This two-step mechanism reduces the energy requirements to below the measurement suggesting that the production of SiH^+ also involves "fragmentation," followed by ionization.

The fragment species not containing silicon (i.e., H and H_2) appear at lower energies than measured for other processes. A potential of only 12.19 eV was measured for H_2^+, which is lower than the molecular ionization potential known to be 15.45 eV. It has not been observed until 24.3 eV in the electron impact of silane [16]. The measured potential for H^+ is only 11.59 eV, whereas the ionization potential of H is 13.5984 eV. The electron impact of silane requires 24.5 eV [16]. Our measurements are significantly lower in energy, again justified by the ultrashort ionization pulse causing fragmentation before the molecule has time to fully relax to the bent state. Figure 6 shows the calculated potential energy

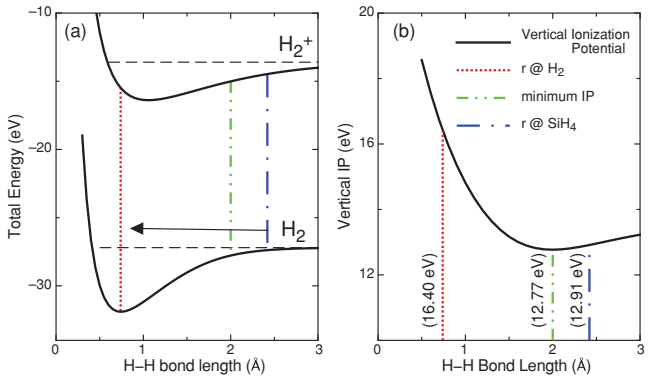

FIG. 6. (Color online) (a) Potential energy curves for H_2 and H_2^+ demonstrate the vertical ionization potential as a function of bond distance. Excitation of the ground state of silane introduces a bending that brings two dangling hydrogen atoms closer together as indicated by the arrow. (b) The solid (black) line demonstrates the difference in energy between the two ion states. The far right, vertical (blue) line demonstrates the distance of two hydrogen atoms in the ground-state geometry of silane (2.42 Å), and the dotted (red) line indicates the vertical ionization potential of the ground state of H_2 (0.74 Å). The minimum vertical energy requirement is around 12.77 eV (∼2.00 Å) as shown with the vertical center (green) line.

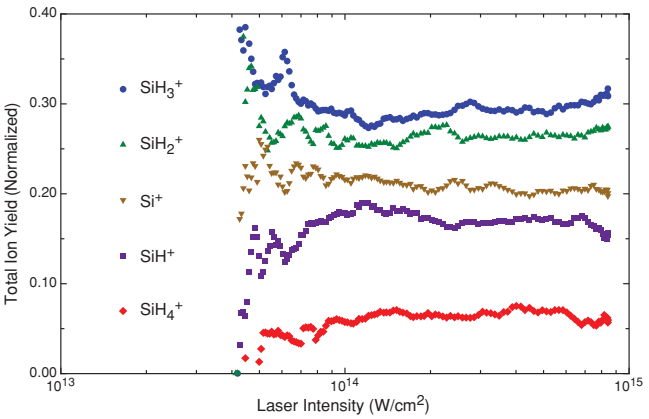

FIG. 7. (Color online) The branching ratios of molecular silane as a function of laser intensity. The signal was normalized to only include species containing an Si atom. Ion signal begins around 5×10^{13} W/cm^2 and remains nearly constant above a laser intensity of 7×10^{13} W/cm^2. This shows that the dominant ion channel is the SiH_3 ion. The ratios are 6, 30, 27, 16, and 20% for SiH_4^+, SiH_3^+, SiH_2^+, SiH^+, and Si^+, respectively.

curve for both the neutral and cation species of molecular hydrogen as the bond length is varied. The ground-state structure of silane has all H-H distances at 2.42 Å, which corresponds to a vertical ionization potential for H_2 to be only 12.91 eV. However, at this distance there is almost no attractive potential between the hydrogen nuclei and it is unlikely they combine. The adiabatic ionization potential is only 11.00 eV at this long distance. As the H-H distance shortens to ∼2.00 Å, the vertical ionization potential drops to a minimum value of 12.77 eV, but the adiabatic value increases to 11.40 eV. This is very close to our measured energy requirements for H^+, 11.59 eV. At an even shorter bond distances, it the attractiveness between the two nuclei becomes stronger and therefore the formation of H_2^+ becomes more probable. However, as the bond shrinks, the adiabatic value increases until finally reaching the known ionization potential of the molecule. This simplified mechanism shows that the unique structure of silane allows for the energy requirements to be lowered for the production of H_2 and H cations. The increase in the adiabatic energy requirement as bonding becomes more probable also explains why the measurement for H_2^+ was larger than for H^+.

C. Branching ratios

The observation of the cation of silane is absent in many electron-impact ionization experiments [17]. This can be attributed to the fact that the dissociation energy of SiH_4^+ is only 0.57 eV [20]. Therefore, the dissociation rate into neutrals is expected to be an order of magnitude larger than the ionization rate [15]. This is consistent with our data where the measured ionization to fragmentation ratio remains constant at roughly 6%, indicating fragmentation is 16.7 times more likely than ionization.

The overall ion signal has been used to measure the branching ratios of molecular silane as a function of pulse energy and is plotted in Fig. 7. To ensure that our measurements are not being skewed by pathways involving secondary ionization, only ions containing Si are included. Above the saturation intensity of silane (∼7×10^{13} W/cm^2), the ion ratios remain roughly constant and are listed in Table II. The most dominant channel is the production of SiH_3^+ at ∼30%. SiH_2^+ is next at roughly 27%, followed by Si^+, SiH^+, and finally SiH_4^+ at 20%, 18%, and 6%, respectively. This is in stark contrast to electron impact experiments where the SiH_2^+ signal dominates and SiH_4^+ is not observed [16,17,19]. The product formation of SiH_2 and SiH_3 through electron-impact ionization is around 70% and 30%, respectively. Single photon ionization of molecular silane at 148 nm (8.4 eV) shows a fragmentation product of SiH_2 of 83%, and SiH_3 at 17% [15].

The frozen ground-state geometry of silane has a vertical energy barrier of 7.34 eV to fragmentation resulting in SiH_2 and H_2, but only 4.14 eV to form SiH_3 and H as demonstrated in Table I. As silane absorbs energy from the laser pulse, two of the dangling hydrogen atoms will come together leading to the expected fragmentation pathway of SiH_4 into SiH_2 and H_2. The fragmentation energy for the loss of H_2 is lowered from 7.34 eV to only 2.62 eV as the H-Si-H bond angle reduces bringing the hydrogen atoms together to the ground state H_2 bond length of 0.74 Å. The adiabatic value for the loss of an atomic hydrogen remains almost constant at ∼4.14 eV. The cation SiH_4^+ relaxes to a geometry with two hydrogen atoms separated by only 0.94 Å, and having a dissociation energy to form SiH_2^+ and H_2 of 0.57 eV. This demonstrates that an ultrafast laser will lead to the preferential loss of atomic hydrogen, but a slower ionization method would preferentially lose H_2 after silane fully rearranges to the bent geometry. The ultrafast laser used in this experiment does not allow for complete relaxation, whereas past studies have measured adiabatic processes. The ultrafast ionization observed in this experiment could explain the enhancement in the production of the SiH_3 ion.

V. CONCLUSION

We have given a detailed description of MO-ADK for a molecule with T_d point group symmetry. For the laser intensities used in this experiment, the ADK ionization signal is in agreement with the molecular orbital calculation. Therefore, the strong field ionization of this T_d molecule can be approximated as if a spherical partial wave.

We have demonstrated that the ionization potential of even a fairly unstable molecule, silane, can be described accurately with both MPI and TI models. Specifically, we stress the accuracy of the MO-ADK or ADK model for describing ionization dynamics. The observed ionization potential of silane is in excellent agreement with its vertical ionization potential. Both of these models have been applied to the fragments of silane and have been found to describe the appearance potentials accurately. MPI observations of the fragments indicate instantaneous, or vertical, excitations, whereas TI is described under adiabatic excitation. Therefore, nuclear rearrangement is significant in strong field ionization mechanisms, even when induced with a femtosecond laser.

Multiply charged species were not observed in the mass spectrum, even with laser intensities as high as $\sim 1 \times 10^{15}$ W/cm^2. Fragmentation was found to be almost 20 times more probable than ionization. Product ratios are maintained almost constant above an intensity of 7×10^{13} W/cm^2. The dominant fragmentation channel and ion product of silane through interaction with a femtosecond laser is SiH_3^+ which is predicted to be the most important ion in the production of *a*-Si:H films. The enhancement in the concentration of SiH_3^+ is attributed to the ultrafast ionization rate of the femtosecond laser.

ACKNOWLEDGMENT

The authors gratefully acknowledge funding provided by the Department of Energy (DOE) Grant No. DE-FG02-92ER14258.

[1] S. Augst, D. Strickland, D. D. Meyerhofer, S. L. Chin, and J. H. Eberly, Phys. Rev. Lett. **63**, 2212 (1989).
[2] A. Talebpour, A. D. Bandrauk, K. Vijayalakshmi, and S. L. Chin, J. Phys. B: At. Mol. Opt. Phys. **33**, 4615 (2000).
[3] J. Purnell, S. Wei, S. A. Buzza, and A. W. Castleman Jr., J. Phys. Chem. **97**, 12530 (1993).
[4] D. A. Card, E. S. Wisniewski, D. E. Folmer, and A. W. Castleman Jr., J. Chem. Phys. **116**, 3554 (2002).
[5] E. M. Snyder, S. A. Buzza, and A. W. Castleman Jr., Phys. Rev. Lett. **77**, 3347 (1996).
[6] E. S. Wisniewski, J. R. Stairs, and A. W. Castleman Jr., Int. J. Mass Spectrom. **212**, 273 (2001).
[7] E. M. Snyder, S. Wei, J. Purnell, S. A. Buzza, and A. W. Castleman Jr., Chem. Phys. Lett. **248**, 1 (1996).
[8] J. V. Ford, L. Poth, Q. Zhong, and A. W. Castleman Jr., Int. J. Mass Spectrom. **192**, 327 (1999).
[9] J. V. Ford, Q. Zhong, L. Poth, and A. W. Castleman Jr., J. Chem. Phys. **110**, 6257 (1999).
[10] D. E. Blumling, S. G. Sayres, and A. W. Castleman Jr., Int. J. Mass Spectrom. (2010), doi:10.1016/j.ijms.2010.07.002.
[11] P. G. Le Comber and W. E. Spear, Phys. Rev. Lett. **25**, 509 (1970).
[12] A. Matsuda, Plasma Phys. Controlled Fusion **39**, A431 (1997).
[13] P. Kae-Nune, J. Perrin, J. Guillon, and J. Jolly, Plasma Sources Sci. Technol. **4**, 250 (1995).
[14] Y. Nozaki, K. Kongo, T. Miyazaki, M. Kitazoe, K. Horii, H. Umemoto, A. Masuda, and H. Matsumura, J. Appl. Phys. **88**, 5437 (2000).
[15] G. Turban, Y. Catherine, and B. Grolleau, Plasma Chem. Plasma Process. **2**, 61 (1982).
[16] R. Basner, M. Schmidt, V. Tarnovsky, K. Becker, and H. Deutsch, Int. J. Mass Spectrom. Ion Processes **171**, 83 (1997).
[17] H. Chatham, D. Hils, R. Robertson, and A. Gallagher, J. Chem. Phys. **81**, 1770 (1984).
[18] J. Perrin, O. Leroy, and M. C. Bordage, Contrib. Plasma Phys. **36**, 3 (1996).
[19] P. Potzinger and F. W. Lampe, J. Phys. Chem. **73**, 3912 (1969).
[20] R. K. Janev and D. Reiter, Contrib. Plasma Phys. **43**, 401 (2003).
[21] D. L. Staebler and C. R. Wronski, Appl. Phys. Lett. **31**, 292 (1977).
[22] L. V. Keldysh, Sov. Phys. JETP **20**, 1307 (1965).
[23] M. Uiberacker *et al.*, Nature (London) **446**, 627 (2007).
[24] S. M. Hankin, D. M. Villeneuve, P. B. Corkum, and D. M. Rayner, Phys. Rev. A **64**, 013405 (2001).
[25] M. V. Ammosov, N. B. Delone, and V. P. Krainov, Sov. Phys. JETP **64**, 1191 (1986).
[26] S. M. Hankin, D. M. Villeneuve, P. B. Corkum, and D. M. Rayner, Phys. Rev. Lett. **84**, 5082 (2000).
[27] M. Smits, C. A. de Lange, A. Stolow, and D. M. Rayner, Phys. Rev. Lett. **93**, 213003 (2004).
[28] C. Guo, Phys. Rev. Lett. **85**, 2276 (2000).
[29] M. J. DeWitt, B. S. Prall, and R. J. Levis, J. Chem. Phys. **113**, 1553 (2000).
[30] J. Muth-Böhm, A. Becker, and F. H. M. Faisal, Phys. Rev. Lett. **85**, 2280 (2000).
[31] X. M. Tong, Z. X. Zhao, and C. D. Lin, Phys. Rev. A **66**, 033402 (2002).
[32] A. A. A. El-Zein *et al.*, Phys. Scr., T **92**, 119 (2001).
[33] P. Hansch and L. D. Van Woerkom, Opt. Lett. **21**, 1286 (1996).
[34] J. Mckenna *et al.*, Phys. Rev. A **73**, 043401 (2006).
[35] P. Hansch, M. A. Walker, and L. D. Van Woerkom, Phys. Rev. A **54**, R2559 (1996).
[36] M. A. Walker, P. Hansch, and L. D. Van Woerkom, Phys. Rev. A **57**, R701 (1998).
[37] W. C. Wiley and I. H. McLaren, Rev. Sci. Instrum. **26**, 1150 (1956).
[38] J. A. Arnaud, W. M. Hubbard, G. D. Mandeville, B. de la Claviere, E. A. Franke, and J. M. Franke, Appl. Opt. **10**, 2775 (1971).
[39] M. J. Frisch *et al.*, *Gaussian 03, Revision E.01*.
[40] A. D. Becke, J. Chem. Phys. **98**, 5648 (1993).
[41] J. P. Perdew, J. A. Chevary, S. H. Vosko, K. A. Jackson, M. R. Pederson, D. J. Singh, and C. Fiolhais, Phys. Rev. B **46**, 6671 (1992).

[42] J. Cizek, in *Advances in Chemical Physics*, edited by P. C. Hariharan, (Wiley Interscience, New York, 1969), Vol. 14, p. 35.
[43] G. D. Purvis and R. J. Bartlett, J. Chem. Phys. **76**, 1910 (1982).
[44] G. E. Scuseria, C. L. Janssen, and H. F. Schaefer III, J. Chem. Phys. **89**, 7382 (1988).
[45] G. E. Scuseria and H. F. Schaefer III, J. Chem. Phys. **90**, 3700 (1989).
[46] U. Varetto, MOLEKEL 5.3; Swiss National Supercomputing Centre, Manno, Switzerland, 2008.
[47] D. M. Brink and G. R. Satchler, *Angular Momentum* (Oxford University Press, London, 1968).
[48] R. N. Zare, *Angular Momentum* (Wiley, New York, 1988).
[49] T. K. Kjeldsen and L. B. Madsen, J. Phys. B: At. Mol. Opt. Phys. **37**, 2033 (2004).
[50] T. K. Kjeldsen, C. Z. Bisgaard, and L. B. Madsen, Phys. Rev. A **71**, 013418 (2005).
[51] T. K. Kjeldsen and L. B. Madsen, Phys. Rev. A **74**, 023407 (2006).
[52] See supplementary material at [http://link.aps.org/supplemental/10.1103/PhysRevA.82.033424], for the complex fitting coefficients of the three molecular orbitals discussed.
[53] P. Lambropoulos, Adv. At. Mol. Phys. **12**, 87 (1976).
[54] J. R. Stairs, S. J. Peppernick, K. M. Davis, and A. W. Castleman Jr., Isr. J. Chem. **44**, 223 (2004).
[55] B. Walker, B. Sheehy, L. F. DiMauro, P. Agostini, K. J. Schafer, and K. C. Kulander, Phys. Rev. Lett. **73**, 1227 (1994).
[56] L. A. Lompré, A. L'Huillier, G. Mainfray, and C. Manus, Phys. Lett. A **112**, 319 (1985).
[57] K. Börlin, T. Heinis, and M. Jungen, Chem. Phys. **103**, 93 (1986).
[58] F. E. Saalfeld and H. J. Svec, Inorg. Chem. **2**, 46 (1963).
[59] G. Cooper, T. Ibuki, and C. E. Brion, Chem. Phys. **140**, 133 (1990).
[60] L. E. Machado, M. T. Lee, and L. M. Brescansin, J. Chem. Phys. **110**, 7228 (1999).
[61] J. Berkowitz, J. P. Greene, H. Cho, and B. Ruščić, J. Chem. Phys. **86**, 1235 (1987).
[62] R. Roberge, C. Sandorfy, J. I. Matthews, and O. P. Strausz, J. Chem. Phys. **69**, 5105 (1978).
[63] A. W. Potts and W. C. Price, Proc. R. Soc. London A **326**, 165 (1972).
[64] A. R. Porter, M. D. Towler, and R. J. Needs, Phys. Rev. B **64**, 035320 (2001).